J Sol-Gel Sci Technol (2017) 82:509–518
DOI 10.1007/s10971-017-4332-0

ORIGINAL PAPER: SOL-GEL AND HYBRID MATERIALS FOR CATALYTIC, PHOTOELECTROCHEMICAL AND SENSOR APPLICATIONS

Enhanced photocatalytic performance and mechanism of Ag-decorated $LaFeO_3$ nanoparticles

Yongchun Ye[1] · Hua Yang[1] · Ruishan Li[1] · Xiangxian Wang[1]

Received: 20 November 2016 / Accepted: 6 February 2017 / Published online: 27 February 2017

Abstract Spherical $LaFeO_3$ nanoparticles with an average size of 35 nm were synthesized by a polyacrylamide gel route. Ag nanoparticles of 8–18 nm in size were decorated onto $LaFeO_3$ particle surface by a chemical reduction method to yield Ag–$LaFeO_3$ composites. The samples were characterized by X-ray powder diffraction, scanning electron microscopy, transmission electron microscopy, ultraviolet–visible diffuse reflectance spectroscopy, and photoluminescence spectroscopy. It is found that $LaFeO_3$ particles have two bandgap energies of 2.59 and 2.24 eV, which undergo almost no change when decorated with Ag nanoparticles. photoluminescence spectra demonstrate that the decoration of $LaFeO_3$ particles with Ag nanoparticles leads to a decreased recombination rate of photogenerated electrons and holes. The photocatalytic activity of the samples was evaluated by degrading Rhodamine B under simulated-sunlight irradiation. Compared to bare $LaFeO_3$ particles, Ag–$LaFeO_3$ composites exhibit an obviously enhanced photocatalytic activity. The formed •OH was examined by photoluminescence spectroscopy using terephthalic acid as the •OH scavenger, revealing an enhanced yield on the irradiated Ag–$LaFeO_3$ composites. To clarify the role of active species in the photocatalysis, the effect of ammonium oxalate (h^+ scavenger), ethanol (•OH scavenger), benzoquinone (•O_2^- scavenger), and N_2 on the Rhodamine B degradation as well as the •OH yield was investigated. Based on the experimental results, •OH and •O_2^- are suggested to be the main active species causing the dye degradation.

Graphical Abstract

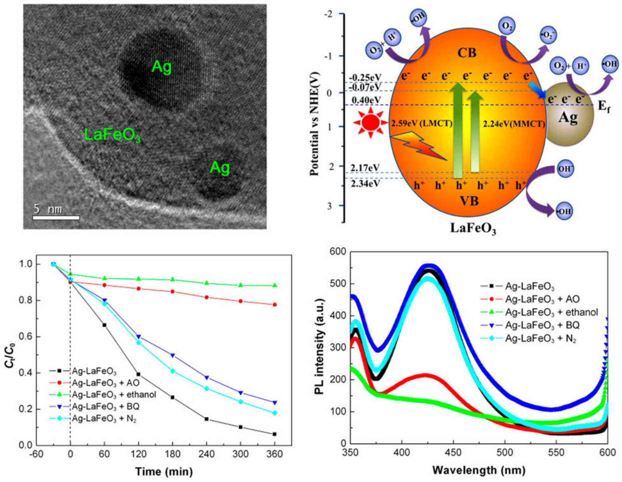

Keywords $LaFeO_3$ nanoparticles · Ag-$LaFeO_3$ composites · Polyacrylamide gel route · Active species · Photocatalytic mechanism

1 Introduction

With the ever-growing demand for paper, textile, paint and cosmetic products, a proportional increase in generation of wastewater containing various organic dyes has been observed simultaneously. It is estimated that every year more than one million tons of organic dyes are produced by chemical industries all over the world. Most of the organic

---

✉ Hua Yang
hyang@lut.cn

[1] School of Science, Lanzhou University of Technology, Lanzhou 730050, People's Republic of China

dyes have a complicated polyaromatic structure, and are hardly decomposed by self-purification action. The organic dyes in wastewater must be removed or destroyed into harmless inorganic substances before being released into the natural environment. Solar energy is an abundant, inexhaustible, non-polluting, and free source of energy. How to utilize solar energy to decompose dye pollutants has become an important research subject in the field of dye wastewater treatment. Among various dye wastewater treatment technologies, semiconductor-based photocatalysis has received a great interest because it allows the use of solar energy for the decomposition of dye pollutants. When a semiconductor is irradiated with light having an energy greater than its E_g, electrons (e^-) are excited from the valence band (VB) to the conduction band (CB), leaving behind holes (h^+) in the VB. The photogenerated electrons and holes migrate to the semiconductor surface, and participate in a series of reduction and oxidation reactions, thus leading to the decomposition of dye pollutants. Efficient separation of e^-–h^+ pairs is one of the key points to achieve a good photocatalytic activity of the semiconductor. Furthermore, development of visible-light-responsive photocatalysts is crucial for the effective utilization of sunlight and hence the industrial application of photocatalytic technology.

In recent years, a great deal of interest has been devoted to perovskite-type photocatalysts, particularly including rare-earth orthoferrites $RFeO_3$ (where R represents rare earth elements) because of their promising photocatalytic properties [1–24]. Generally, rare-earth orthoferrites such as $CeFeO_3$ [3], $PrFeO_3$ [4], $SmFeO_3$ [5], $YFeO_3$ [6, 7], $GdFeO_3$ [8, 9], $TbFeO_3$ [10], $LuFeO_3$ [11], and $LaFeO_3$ [12–24] have a relatively small bandgap energy of 2.0–2.6 eV compared to the well-known TiO_2 photocatalyst with a bandgap energy of 3.2 eV, making them attractive as efficient visible-light-responsive photocatalysts. As one of the representatives of rare-earth orthoferrites, $LaFeO_3$ with an orthorhombic perovskite-type structure is particularly interesting. Since the discovery of the photocatalytic degradation of Rhodamine B (RhB) aqueous solution and photocatalytic decomposition of water into hydrogen over $LaFeO_3$ under visible-light irradiation [12, 13], $LaFeO_3$ has been extensively studied as a promising visible-light driven photocatalyst [14–25].

It is well established that the overall photocatalytic activity of a photocatalyst depends on numerous factors including its crystalline phase, morphology, microstructure and surface area. Effectively suppressing the recombination of photogenerated electrons, and holes is crucial to achieve a good photocatalytic activity of the photocatalyst. One of the promising strategies for achieving this goal is through the decoration of the photocatalyst with noble metal (e.g. Ag, Au, Pt, etc.) [26–28]. When the photocatalyst is decorated by noble metal particles, electrons generated in the irradiated photocatalyst are expectedly captured by noble metal particles that act as efficient electron sinks, leaving behind holes on the photocatalyst surface. As a result, photogenerated holes are increasingly available to participate in photocatalytic reactions. Li et al. fabricated the ribbon-like porous Ag/$LaFeO_3$ nanobelt photocatalyst via electrospinning, and found that the composite photocatalyst exhibited enhanced photocatalytic performance compared to bare $LaFeO_3$ [29]. However, a more detailed investigation on the involved photocatalytic mechanism is still indispensable. In this study, we adopted a polyacrylamide gel route as described in the literature [30] to synthesize $LaFeO_3$ nanoparticles. Ag nanoparticles were assembled onto the surface of $LaFeO_3$ particles via a chemical reduction method to yield Ag–$LaFeO_3$ nanocomposites. The photocatalytic performance and mechanism of the as-prepared Ag–$LaFeO_3$ photocatalyst was investigated by the degradation of RhB under simulated-sunlight irradiation.

2 Experimental

2.1 Preparation of $LaFeO_3$ particles

All raw materials and chemical reagents used in the synthesis of $LaFeO_3$ particles were of analytical grade without further purification. 0.0075 mol of $La(NO_3)_3$ and 0.0075 mol of $Fe(NO_3)_3$ were dissolved in 20 mL of dilute nitric acid solution. Then to the solution were successively added 0.0225 mol of citric acid (i.e., 1.5 times the amount of total La^{3+}/Fe^{3+} ions), 20 g of glucose, and 0.135 mol of acrylamide (i.e., 9 times the amount of total La^{3+}/Fe^{3+} ions). Every step mentioned above was accompanied by a constant magnetic stirring to make the additives dissolve completely. The mixture solution was made up to 100 mL by adding distilled water and then heated at 80 °C on a hot plate to initiate the polymerization reaction. After 4 h of reaction, the mixture solution was translated into a gel. The obtained gel was dried at 120 °C for 24 h in a thermostat drier. The formed xerogel was ground into powder and submitted to calcination in a tubular furnace at 500 °C for 3 h. After the tubular furnace was cooled down to room temperature naturally, $LaFeO_3$ nanoparticles were obtained.

2.2 Deposition of Ag onto $LaFeO_3$ particles

Ag nanoparticles were deposited onto $LaFeO_3$ particles by a chemical reduction method. 0.1 g of $LaFeO_3$ particles was dispersed in 20 mL of absolute ethyl alcohol, and then the suspension was ultrasonically treated for 30 min. 0.2 mL of $AgNO_3$ solution with a concentration of 0.2 mol L^{-1} (M) was added to the suspension under magnetic stirring in ice-water bath. To the mixture was slowly added 1.84 mL of 0.1 M $NaBH_4$ solution drop by drop under quick stirring, during which time Ag^+ ions were reduced to form small Ag particles onto the surface of $LaFeO_3$ particles. The involved chemical reaction can be described by Eq. (1). After full deposition of Ag nanoparticles for another 20 min, the precipitate was collected and washed several times with distilled water, and then submitted to drying in a thermostat drying oven at 60 °C for 4 h to obtain Ag–$LaFeO_3$ composite particles.

$$\begin{aligned} 2AgNO_3 + 4NaBH_4 + 10H_2O \rightarrow 2Ag + 2NH_3 \\ +4NaOH + 4B(OH)_3 + 7H_2 \end{aligned} \tag{1}$$

2.3 Sample characterization

The crystal structure of the samples was determined by means of X-ray powder diffraction (XRD) with Cu Kα radiation ($\lambda = 0.15406$ nm). The morphology and microstructure of the samples was investigated by field-emission scanning electron microscopy (SEM) and field-emission transmission electron microscopy (TEM). The ultraviolet (UV)-visible diffuse reflectance spectrum of the samples was measured on a UV–visible spectrophotometer with an integrating sphere attachment by using $BaSO_4$ as the reference. The photoluminescence (PL) spectra of the samples were measured on a fluorescence spectrophotometer with the excitation wavelength of 315 nm.

2.4 Photocatalytic evaluation

The photocatalytic activity of the samples was evaluated by degrading RhB in aqueous solution under simulated-sunlight irradiation from a 200 W xenon lamp (solar simulator). The initial concentration of RhB was 2 mg L^{-1} and the photocatalyst loading was 0.1 g in 100 mL of RhB solution. Before photocatalysis, the suspension was magnetically stirred for 30 min in the dark in order to attain the adsorption/desorption equilibrium of RhB onto the photocatalyst surface. During the photocatalysis process, the reaction solution was kept at room temperature by cooling the photocatalytic reactor with a water-cooling system. At given intervals of time, a small amount of the reaction solution was taken out to measure the concentration of RhB. Before measurement the photocatalyst particles were removed by centrifuging at 4000 r min^{-1} for 10 min. The RhB concentration was determined by measuring the absorbance of the solution at a fixed wavelength of $\lambda = 554$ nm using a UV-visible spectrophotometer. The degradation efficiency is defined as $(C_0 - C_t)/C_0 \times 100\%$, where C_0 and C_t represent the initial RhB concentration and the remaining RhB concentration after photocatalysis for time t, respectively.

2.5 Detection of hydroxyl (•OH)

•OH formed over the simulated-sunlight-irradiated photocatalyst was examined by PL spectroscopy using terephthalic acid (TPA) as the •OH scavenger. TPA tends to react with •OH to produce 2-hydroxyterephthalic acid (TAOH) that is a highly fluorescent compound exhibiting characteristic PL at around 429 nm. The PL intensity is in proportion to the amount of produced •OH. TPA solution with a concentration of 0.25 mmol L^{-1} was prepared by dissolving TPA in a 1.0 mmol L^{-1} NaOH solution. 0.1 g of the photocatalyst was added to 100 mL of the TPA solution. After magnetically stirred for 30 min in the dark, the mixed solution was irradiated by a 200 W xenon lamp. After reaction for a certain period of time, a small portion of the reaction solution was pipetted out and centrifuged at 4000 r min^{-1} for 10 min to remove the photocatalyst. The upper clear solution in the centrifuge tube was used for the PL measurement at a fluorescence spectrophotometer with the excitation wavelength of 315 nm.

3 Results and discussion

Figure 1 shows the XRD patterns of $LaFeO_3$ particles and Ag–$LaFeO_3$ composites, along with the standard XRD line pattern for $LaFeO_3$ orthorhombic structure (PDF card No. 037-1493). For bare $LaFeO_3$ particles, all the diffraction peaks can be well indexed according to the standard

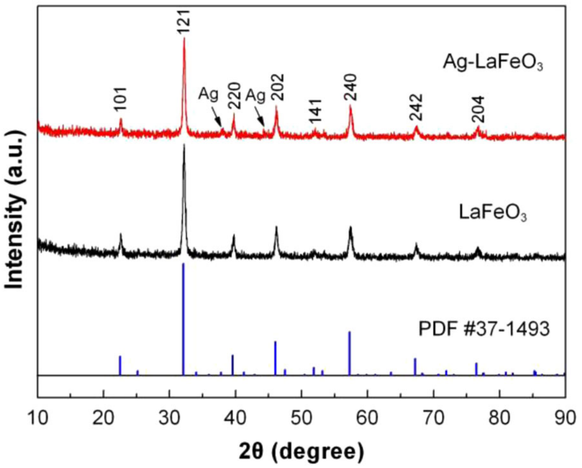

Fig. 1 XRD patterns of $LaFeO_3$ particles and Ag-$LaFeO_3$ composites, along with the standard XRD line pattern for $LaFeO_3$ orthorhombic structure (PDF card No. 037-1493)

diffraction pattern of $LaFeO_3$, implying the formation of single orthorhombic perovskite phase. For Ag–$LaFeO_3$ composites, additional weak diffraction peaks assignable to Ag are visible in the XRD pattern, indicating the formation of Ag onto $LaFeO_3$ particles. Furthermore, from the XRD pattern $LaFeO_3$ particles are seen to undergo no structural change when decorated with Ag nanoparticles.

Figure 2a shows the SEM image of $LaFeO_3$ particles, revealing that the particles are regularly shaped like spheres. Figure 2b gives the statistical estimation of the primary particle size distribution (measured by Heywood diameter). It is seen that the particle size distribution ranges from 20 to 60 nm and 70% of the particles have a size in the range of 30–40 nm. The average size of the particles is estimated to be 35 nm.

The microstructure of Ag-decorated $LaFeO_3$ particles was investigated by TEM. Figure 3a shows the TEM image of Ag–$LaFeO_3$ composites. The dominant particles, identified to be $LaFeO_3$ particles, are spherically shaped with an average size of 35 nm. The morphology and size of $LaFeO_3$ particles observed by TEM basically agrees with that observed from the SEM image. Much smaller-sized particles with size of 8–18 nm are seen to be decorated onto $LaFeO_3$ particles, as indicated by *arrows*, and these ultrafine particles are identified to be Ag nanoparticles. Figure 3b shows the high resolution TEM (HRTEM) image of Ag–$LaFeO_3$ composites, revealing good assembly of Ag nanoparticles onto the surface of $LaFeO_3$ particles. It is clear that Ag nanoparticles display perfect crystal lattice fringes with an interplanar distance of 0.236 nm, which correspond to the (111) crystal plane of Ag. No internal defects are visible in the monocrystalline Ag nanoparticles. Moreover, clear crystal lattice fringes are also observed for $LaFeO_3$ particles, implying that they have a good crystallization. Figure 3c shows the selected area electron diffraction (SAED) pattern of Ag–$LaFeO_3$ composites, clearly presenting polycrystalline diffraction rings. Almost all of the diffraction rings can be indexed in terms of the $LaFeO_3$ orthorhombic structure. Weak diffraction rings or spots assignable to Ag are also visible in the SAED pattern, and as an example, Ag (111) diffraction ring is indicated in the SAED pattern. The SAED result implies that $LaFeO_3$ particles remain in well-crystallized orthorhombic perovskite phase without undergoing structural change when decorated with Ag nanoparticles. Figure 3d shows the high-angle annular dark-field (HAADF) scanning TEM image of Ag–$LaFeO_3$ composites, further revealing that spherical $LaFeO_3$ particles are decorated with ultrafine Ag nanoparticles. The corresponding elemental mapping images of the region indicated in Fig. 3d are given in Fig. 3e. The elements La, Fe and O have a nearly identical distribution, implying no chemical composition segregation in the $LaFeO_3$ phase. The observed uniform distribution of the Ag element suggests that Ag nanoparticles are uniformly assembled onto $LaFeO_3$ particles without aggregation. The chemical composition of Ag–$LaFeO_3$ composites is further confirmed by the energy dispersive analysis of X-ray (EDX) spectrum, as shown in Fig. 3f. Besides the signatures of the constituent elements of $LaFeO_3$ crystals, the signature from Ag element is clearly included in the spectrum. The observed C signature could arise from the microgrid used for supporting the sample. It is noted that EDX is sensitive to heavy elements like La and Fe, but not to light elements like O. This suggests that EDX can be used to precisely determine the content of heavy elements. From the EDX spectrum, the atomic ratio of La to Fe is obtained as 1:1, which is in good agreement with the La/Fe atomic ratio of $LaFeO_3$ phase.

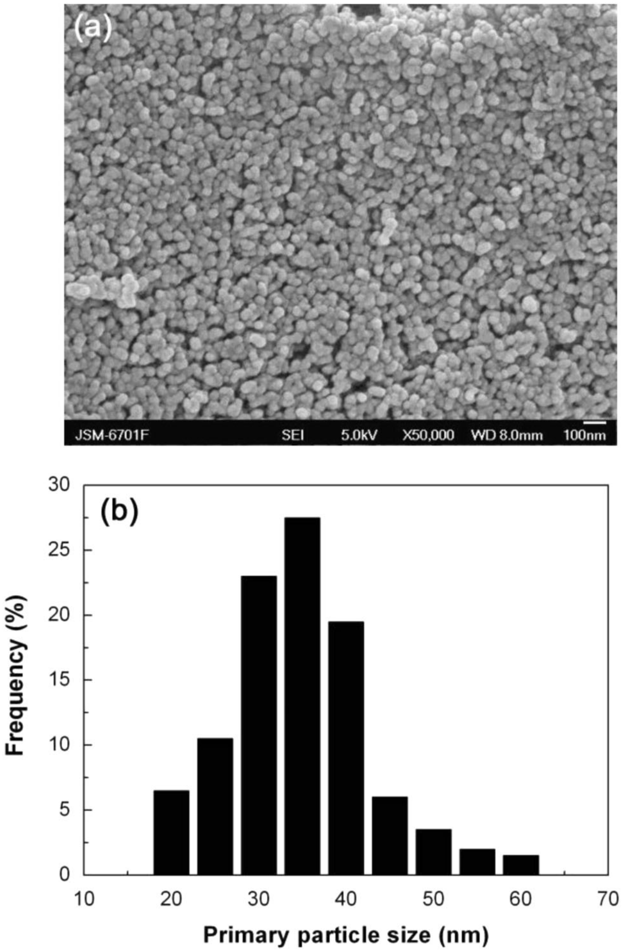

Fig. 2 **a** SEM image of $LaFeO_3$ particles. **b** Statistical estimation of the primary particle size distribution

Figure 4a shows the UV-visible diffuse reflectance spectra of $LaFeO_3$ particles and Ag–$LaFeO_3$ composites. It is seen that the decoration of Ag nanoparticles significantly enhances the visible light absorption of $LaFeO_3$ particles. The bandgap energies of the samples can be obtained from

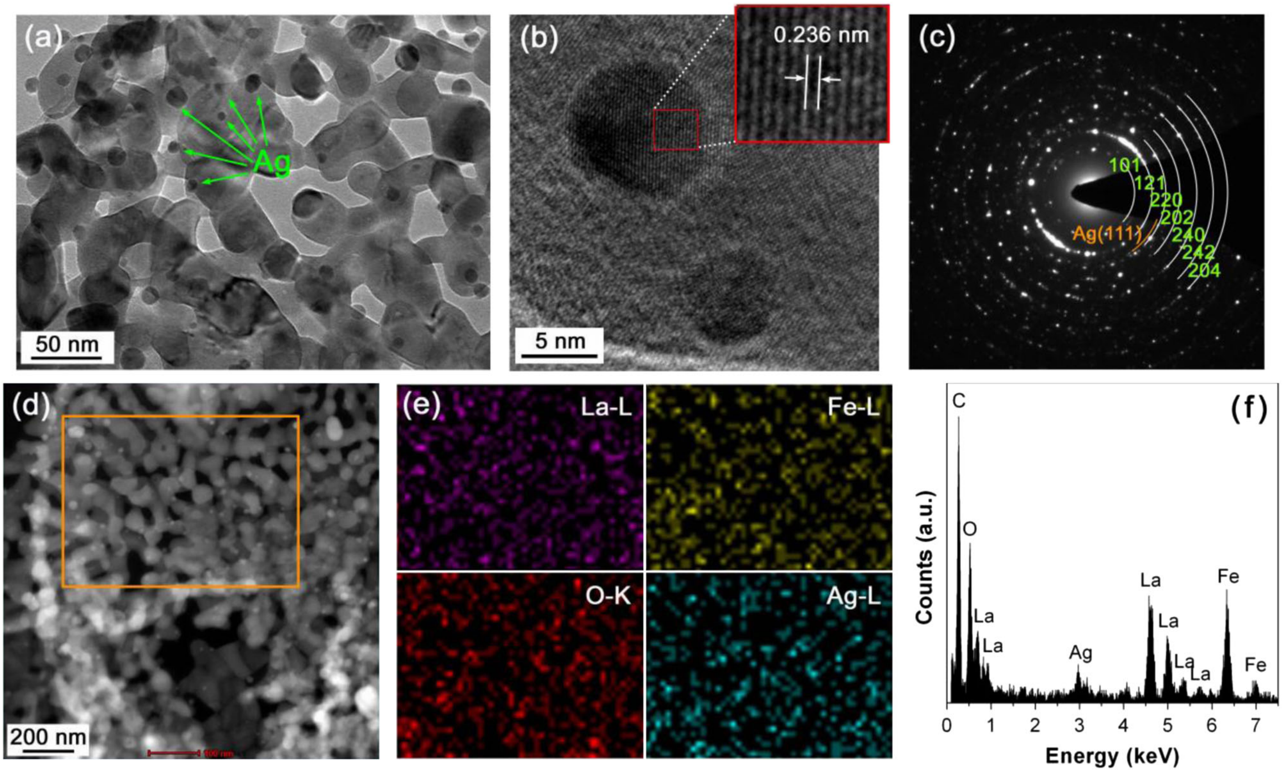

Fig. 3 **a** TEM image of Ag-LaFeO$_3$ composites. **b** HRTEM image of Ag–LaFeO$_3$ composites. **c** SAED pattern of Ag–LaFeO$_3$ composites. **d** HAADF scanning TEM image of Ag–LaFeO$_3$ composites. **e** The corresponding elemental mapping images of the region indicated in (**d**). **f** EDX spectrum of Ag–LaFeO$_3$ composites

the corresponding first derivative spectra as shown in Fig. 4b, where the peak wavelengths are characterized to be the absorption edges of the samples. For LaFeO$_3$ particles, two absorption edges are observed at 478.1 and 554.5 nm, which are attributed to the ligand field transition of Fe^{3+} (i.e., ligand to metal charge transfer, LMCT), and the excitation of two adjacent high-spin Fe^{3+} centers (i.e., metal to metal charge transfer, MMCT), respectively [31]. From the absorption edges, the two bandgap energies of LaFeO$_3$ particles are obtained as 2.59 and 2.24 eV. When decorated with Ag nanoparticles, the two absorption edges of LaFeO$_3$ particles undergo almost no shift, implying a negligible change in their bandgap energies.

To understand the recombination behavior of photogenerated e$^-$–h$^+$ pairs in the photocatalysts, the PL spectra of LaFeO$_3$ particles and Ag–LaFeO$_3$ composites are measured, and the results are shown in Fig. 5. An obvious PL emission peak is observed at around 490 nm, which originates from the recombination of photogenerated electrons and holes. Compared to bare LaFeO$_3$ particles, Ag–LaFeO$_3$ composites have a relatively weak PL intensity, implying that the decoration of LaFeO$_3$ particles with Ag nanoparticles results in a decrease in the e$^-$–h$^+$ recombination. This is ascribed to the effective electron transfer from LaFeO$_3$ to Ag nanoparticles.

Figure 6a shows the photocatalytic degradation of RhB over LaFeO$_3$ particles and Ag-LaFeO$_3$ composites under simulated-sunlight irradiation as a function of irradiation time (*t*). The blank experiment result is also shown in Fig. 6a, revealing that in the absence of the photocatalyst, RhB appears to be stable under simulated-sunlight irradiation and only about 6% of the dye is observed to be degraded after 360 min of irradiation. Before photocatalysis, the adsorption of RhB onto the photocatalyst is measured in the dark at 30 min of contact time. The dye adsorption is obtained as 6 and 10% for LaFeO$_3$ particles and Ag–LaFeO$_3$ composites, respectively. Generally a moderate adsorption of the dye onto the photocatalyst surface favors the photocatalytic reaction because the produced active species responsible for the dye degradation are dominantly located at the photocatalyst surface. On irradiation with simulated-sunlight in the presence of the photocatalyst, RhB undergoes a substantial degradation with increasing the irradiation time, and its percentage degradation reaches 66% for LaFeO$_3$ particles and 94% for Ag–LaFeO$_3$ composites. It is obvious that Ag-decorated LaFeO$_3$ particles exhibit an enhanced photocatalytic activity compared to bare LaFeO$_3$ particles. Figure 6b shows the plots of ln(C_t/C_0) vs. irradiation time (*t*) for LaFeO$_3$ particles and Ag–LaFeO$_3$ composites. It is seen that the photocatalytic degradation of

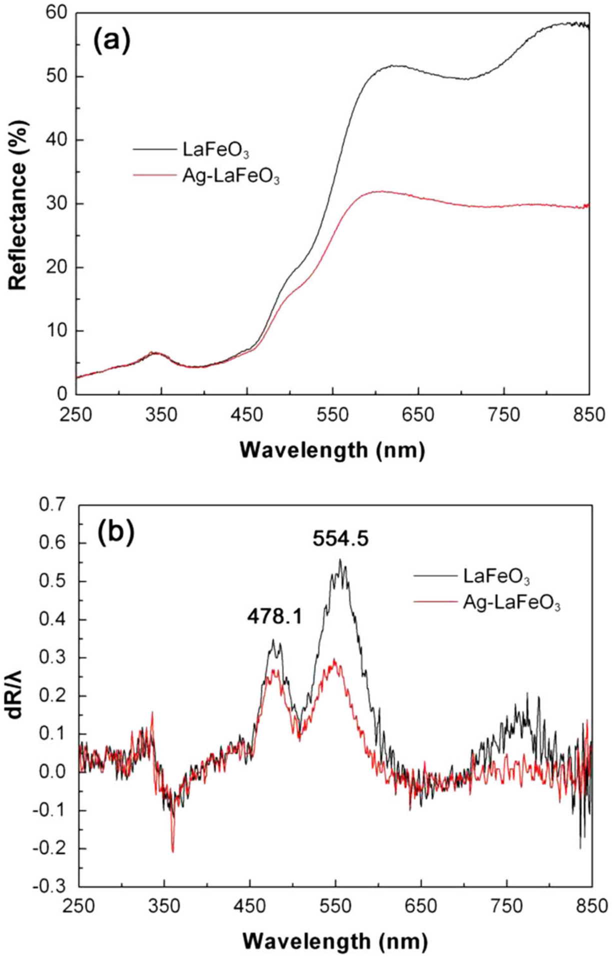

Fig. 4 **a** UV-visible diffuse reflectance spectra of $LaFeO_3$ particles and Ag–$LaFeO_3$ composites. **b** The corresponding first derivative spectra

RhB can be well modeled using the first-order kinetic equation $\ln(C_t/C_0) = -k_{app}t$, where k_{app} is the apparent first-order reaction rate constant (min^{-1}) [32]. The rate constant k_{app} is obtained as 0.00296 min^{-1} for $LaFeO_3$ particles and 0.0078 min^{-1} for Ag–$LaFeO_3$ composites. This implies that the photocatalytic activity of $LaFeO_3$ particles is increased by 1.6 times when decorated with Ag nanoparticles.

In the photocatalysis, the active species responsible for the dye degradation mainly include h^+, •OH, and superoxide (•O_2^-) [33]. To clarify the role of these active species in the photocatalysis, we investigate the effect of ammonium oxalate (AO), ethanol, and benzoquinone (BQ) on the photocatalytic degradation of RhB over Ag–$LaFeO_3$ composites. It is known that AO, ethanol, and BQ can be used as the scavengers of h^+, •OH, and •O_2^-, respectively [34]. Figure 7a shows the time-dependent photocatalytic degradation of RhB by separately adding 0.1 mmol of AO, 10 mL of ethanol, and 0.1 mmol of BQ in 100 mL reaction solution. The degradation percentages of RhB after 360 min irradiation are given in Fig. 7b. It is found that when adding AO and ethanol to the reaction solution, the photocatalytic degradation of RhB is significantly suppressed, only reaching 22 and 12% after 360 min of photocatalysis, respectively. This implies that h^+ and •OH play an important role in the photocatalysis. Considering that h^+ will combine with OH^- and/or H_2O to form •OH, it is concluded that •OH is the dominant active species responsible for the dye degradation. The addition of BQ leads to a slight suppression of the dye degradation, indicating that •O_2^- plays a relatively minor role in the dye degradation. Note that •O_2^- derives from the reaction between dissolved O_2 and photogenerated e^-, and its role on the dye degradation can be further clarified by investigating the effect of N_2 on the photocatalytic efficiency since the dissolved O_2 can be removed from the solution by the N_2-purging procedure. The photocatalytic degradation of RhB under N_2-purging condition is shown in Fig. 7, demonstrating that the dye degradation is slightly suppressed. This result further confirms that •O_2^- plays a relatively minor role for the dye degradation.

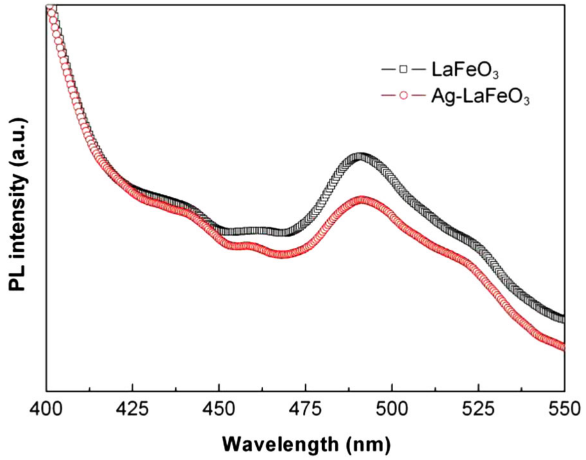

Fig. 5 PL spectra of $LaFeO_3$ particles and Ag–$LaFeO_3$ composites

To reveal the photocatalysis mechanism, we also examine the •OH formed over the simulated-sunlight-irradiated photocatalyst by spectrofluorimetry using TPA as the •OH scavenger. Figure 8a show the PL spectra of the TPA solution reacted for 360 min over $LaFeO_3$ particles and Ag–$LaFeO_3$ composites, along with the blank experiment result. In the absence of the photocatalyst, the TPA solution after 360 min of irradiation shows no PL signal at 429 nm. On irradiation in the presence of $LaFeO_3$ particles or Ag–$LaFeO_3$ composites, the TPA solution shows obvious PL signal centered around 429 nm. This indicates that •OH is produced over the simulated-sunlight-irradiated $LaFeO_3$ and Ag–$LaFeO_3$ photocatalysts. Furthermore, the

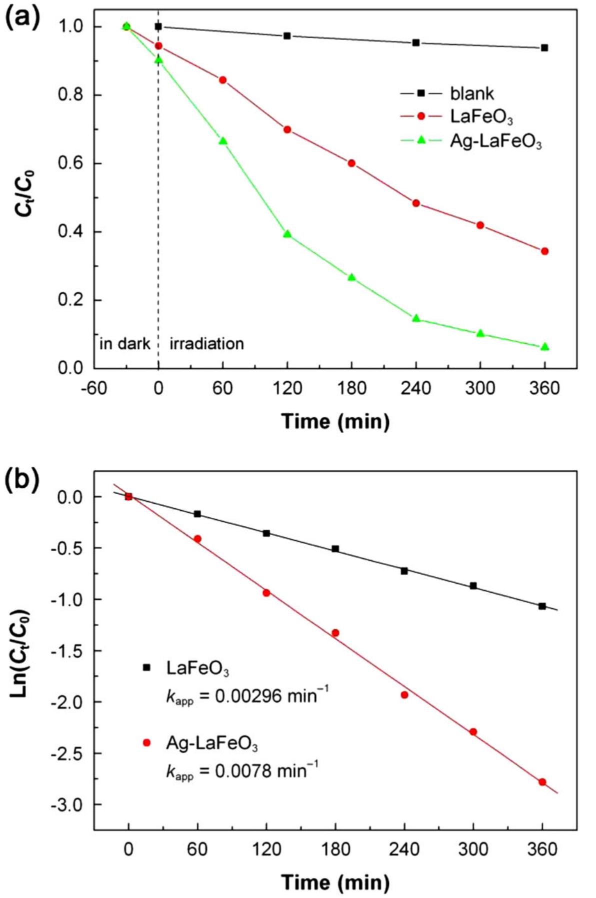

Fig. 6 **a** Time-dependent photocatalytic degradation of RhB over LaFeO$_3$ particles and Ag–LaFeO$_3$ composites under simulated-sunlight irradiation, along with the blank experiment result. **b** Plots of ln(C_t/C_0) vs. irradiation time (t) for LaFeO$_3$ particles and Ag–LaFeO$_3$ composites

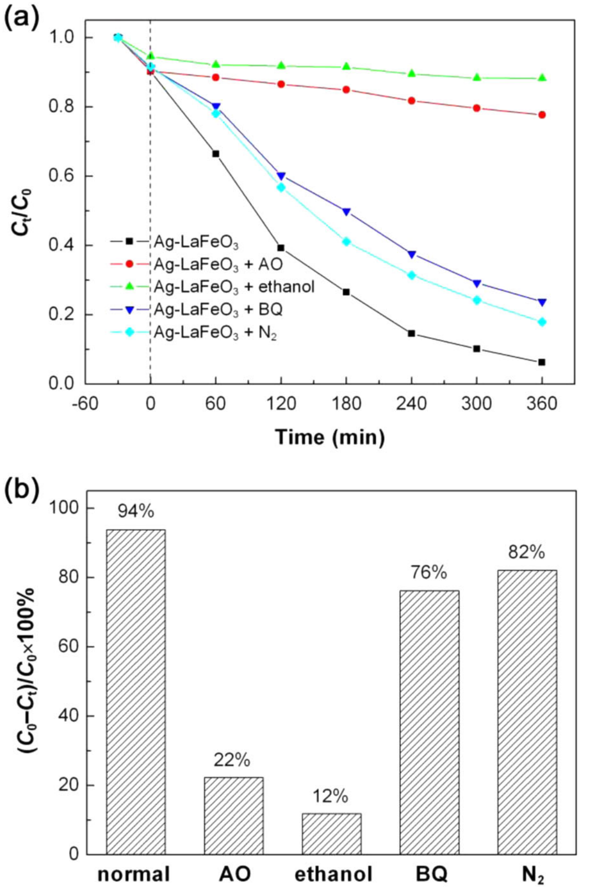

Fig. 7 **a** Effect of AO, ethanol, BQ, and N$_2$ on the time-dependent photocatalytic degradation of RhB over Ag–LaFeO$_3$ composites. **b** The corresponding degradation percentages of RhB after 360 min irradiation

PL signal becomes more intense when Ag–LaFeO$_3$ composites are used as the photocatalyst compared to bare LaFeO$_3$ particles, implying an enhanced yield of •OH over the irradiated Ag-LaFeO$_3$ composites. The enhanced yield of •OH consequently leads to an enhanced photocatalytic activity for Ag-decorated LaFeO$_3$ particles. Figure 8b shows the effect of AO, ethanol, BQ and H$_2$ on the PL spectrum of the TPA solution reacted for 360 min over the simulated-sunlight-irradiated Ag–LaFeO$_3$ composites. When adding ethanol to the TPA reaction solution, the PL signal disappears completely, implying that •OH is quenched by ethanol. On the addition of AO, only a weak PL signal is observed for the TPA solution, indicating a significant decrease in the production of •OH. This is because that the photogenerated h$^+$ is captured by AO, and thus no h$^+$ is available for the generation of •OH. The observed small amount of •OH (determined from the weak PL signal) could derive from the reaction between photogenerated e$^-$ and O$_2$/H$^+$. When adding BQ or purging with N$_2$, the PL signal intensity undergoes a negligible change, indicating that BQ and N$_2$ have almost no effect on the yield of •OH.

Based on the experimental results, a possible photocatalytic mechanism is proposed to elucidate the dye degradation over Ag-decorated LaFeO$_3$ particles, as shown in Fig. 9. When LaFeO$_3$ particles are irradiated with light of energy greater than their E_g, electrons are excited from the VB to the CB, simultaneously creating holes in the VB. Generally, most of the photogenerated carriers recombine quickly, leaving behind only a few carriers participating in the photocatalytic reaction. To achieve a good photocatalytic activity of a semiconductor, it is indispensable to effectively promote the separation of e$^-$–h$^+$ pairs. When LaFeO$_3$ particles are decorated with ultrafine Ag particles, photogenerated electrons tend to migrate from LaFeO$_3$ to Ag particles. The electron transfer process results in a decrease in the recombination rate of e$^-$–h$^+$ pairs, which is evidenced by the PL spectra given in Fig. 5, and as a result, more holes and electrons are available for the photocatalytic reaction. To further understand the photocatalytic

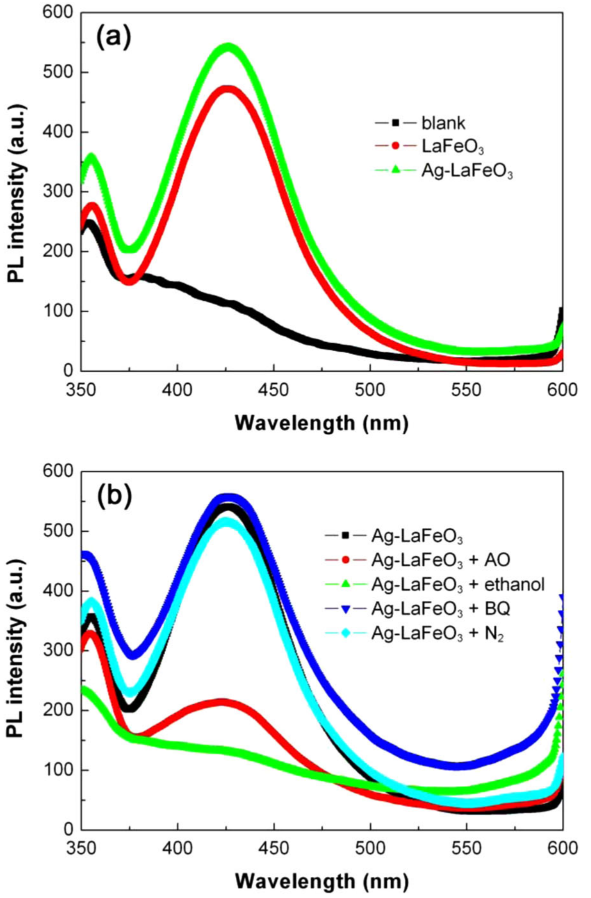

Fig. 8 **a** PL spectra of the TPA solution reacted for 360 min over $LaFeO_3$ particles and Ag–$LaFeO_3$ composites. **b** Effect of AO, ethanol, BQ and H_2 on the PL spectrum of the TPA solution reacted for 360 min over Ag–$LaFeO_3$ composites

mechanism, it is necessary to get the CB and VB edge potentials of $LaFeO_3$ because the redox ability of photogenerated electrons and holes is highly dependent on the energy-band potentials of the photocatalyst. The CB potential of $LaFeO_3$ can be calculated using the following relation [35].

$$
\begin{aligned}
E_{CB} &= X - E^{e} - 0.5E_{g} \\
E_{CB} &= X - E^{e} + 0.5E_{g}
\end{aligned}
\tag{2}
$$

where X is the absolute electronegativity of $LaFeO_3$, E^e is the energy of free electrons on the hydrogen scale (4.5 eV), and E_g is the bandgap energies of $LaFeO_3$ (2.59 eV for LMCT and 2.24 eV for MMCT). The value of X is defined as the arithmetic mean of the electron affinity and the first ionization of the constituent atoms, and estimated to be 5.55 eV for $LaFeO_3$ according to the data reported in literature [36, 37]. The CB and VB potentials of $LaFeO_3$ are therefore calculated to be −0.25/−0.07 V and +2.34/+2.17 V vs. NHE (normal hydrogen electrode), respectively. The CB potential of $LaFeO_3$ is negative to the Fermi level of Ag (+0.4 V vs. NHE [38]), implying that the electron transfer from $LaFeO_3$ to Ag is thermodynamically feasible. Generally, there are two possible paths to produce •OH in the photocatalytic system [11]. One is the oxidative path through combination of the photogenerated-h^+ with OH^- or H_2O, and the other is the reductive path through combination of the photogenerated e^- with O_2/H^+. The redox potentials of OH^-/•OH and H_2O/•OH are +1.89 and +2.72 V vs. NHE [39], which are negative and positive to the VB potential of $LaFeO_3$, respectively. This suggests that, from a thermodynamic point of view, the photogenerated h^+ can react with OH^- (but cannot react with H_2O) to produce •OH. The redox potential of O_2/H_2O_2 (+0.695 V [40]) is positive to the CB potential of $LaFeO_3$ as well as the Fermi level of Ag, and as a result, the photogenerated e^- at both $LaFeO_3$ and Ag can also react with O_2/H^+ to produce •OH. It is noted that on the addition of AO (an h^+ scavenger) to the reaction solution, the yield of •OH is caused to be significantly reduced (Fig. 8b). This indicates that •OH is produced dominantly through the combination of h^+ with OH^-. On the exhaustion of h^+ caused by AO, however, a small amount of •OH is still observed to be generated, and this small portion of •OH is expectedly derived from the combination of e^- with O_2/H^+. The redox potential of O_2/•O_2^- (−0.13 V [41]) is positive to the CB potential of $LaFeO_3$, and thus the photogenerated e^- can react with O_2 dissolved in the reaction solution to produce •O_2^-. This is why the addition of BQ (an •O_2^- scavenger) to the reaction solution or purge with N_2 also has an influence on the photocatalytic degradation of RhB. Based on the experimental results and analysis, •OH and •O_2^- are suggested to be the main active species responsible for the dye degradation. The main reactions involved in the photocatalytic process can be briefly

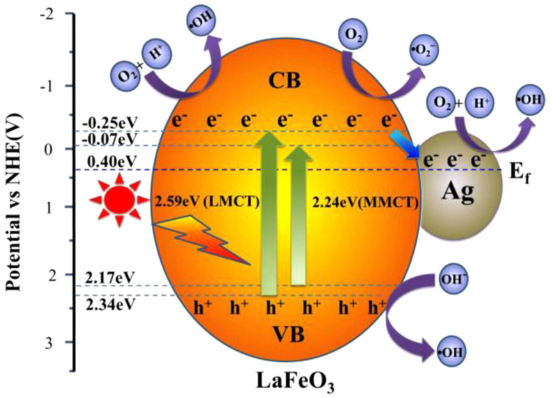

Fig. 9 Schematic illustration of the photocatalytic mechanism of Ag–$LaFeO_3$ composites

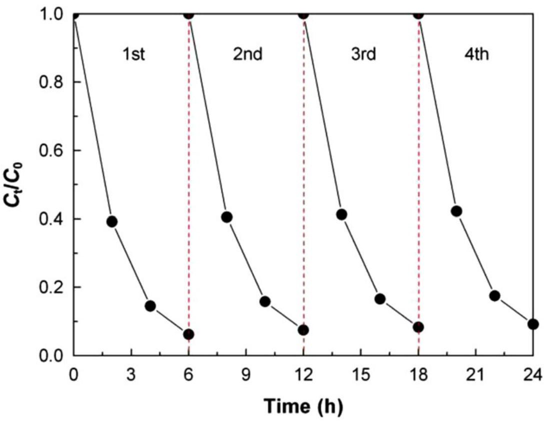

Fig. 10 Photocatalytic degradation of RhB over Ag–$LaFeO_3$ composites during four photocatalytic cycles

described as follows.

$$LaFeO_3 + h\nu \rightarrow LaFeO_3(e^- + h^+) \quad (3)$$

$$h^+ + OH^- \rightarrow \bullet OH \quad (4)$$

$$2e^- + O_2 + 2H^+ \rightarrow H_2O_2 \quad (5)$$

$$e^- + H_2O_2 \rightarrow \bullet OH + OH^- \quad (6)$$

$$e^- + O_2 \rightarrow \bullet {O_2}^- \quad (7)$$

$$\bullet OH, \bullet {O_2}^- + RhB \rightarrow \text{degradation products} \quad (8)$$

We also investigate the photocatalytic stability of Ag–$LaFeO_3$ composites by the recycling photocatalytic experiment. After the first cycle of the photocatalysis was completed, the photocatalyst is collected and washed with water, followed by drying in a thermostat drier. The recovered photocatalyst is introduced to the fresh RhB solution for the next cycle of the photocatalytic experiment under the same conditions. This process is repeated for three times. Figure 10 shows the photocatalytic degradation of RhB over Ag-$LaFeO_3$ composites during the four photocatalytic cycles, revealing an excellent recycling stability of the photocatalyst. At the 4th cycle of the photocatalysis, the RhB degradation still reaches a high value of 91% after irradiation for 6 h.

4 Conclusions

A polyacrylamide gel route was used to synthesize spherical $LaFeO_3$ nanoparticles with an average size of 35 nm. Ag–$LaFeO_3$ composites were prepared by depositing Ag nanoparticles (8–18 nm in size) onto $LaFeO_3$ particle surface through a chemical reduction method. When decorated with Ag nanoparticles, the two bandgap energies of $LaFeO_3$ particles undergo almost no change and are determined to be 2.59 and 2.24 eV. The photocatalytic experiment reveals that Ag-$LaFeO_3$ composites exhibit an enhanced photocatalytic activity toward the RhB degradation under simulated-sunlight irradiation compared to bare $LaFeO_3$ particles. This can be explained by the effective separation of e^-–h^+ pairs due to the e^- transfer from $LaFeO_3$ to Ag nanoparticles and hence the increased availability of carriers for the photocatalytic reaction. On the addition of AO and ethanol to the reaction solution, the RhB degradation is significantly suppressed, while the addition of BQ or purge with N_2 leads to a relatively slight suppression of the dye degradation. Moreover, the addition of AO leads to a significant decrease in the •OH yield, and the addition of ethanol causes the quenching of •OH. Based on the experimental results, •OH and $\bullet {O_2}^-$ are suggested to be the main active species responsible for the dye degradation.

Acknowledgements This work was supported by the National Natural Science Foundation of China (Grant Nos. 51262018 and 51662027).

Compliance with Ethical Standards

Conflict of Interest The authors declare that they have no competing interest.

References

1. Oka M, Miseki Y, Saito K, Kudo A (2015) Photocatalytic reduction of nitrate ions to dinitrogen over layered perovskite $BaLa_4Ti_4O_{15}$ using water as an electron donor. App Catal B-Environ 179:407
2. Maeda K, Domen K (2014) Preparation of $BaZrO_3$-$BaTaO_2N$ solid solutions and the photocatalytic activities for water reduction and oxidation under visible light. J Catal 310:67
3. Ameta J, Kumar A, Ameta R, Sharma VK, Ameta SC (2009) Synthesis and characterization of $CeFeO_3$ photocatalyst used in photocatalytic bleaching of gentian violet. J Iran Chem Soc 6:293
4. Tijare SN, Bakardjieva S, Subrt J, Joshi MV, Rayalu SS, Hishita S, Labhsetwar N (2014) Synthesis and visible light photocatalytic activity of nanocrystalline $PrFeO_3$ perovskite for hydrogen generation in ethanol-water system. J Chem Sci 126:517
5. Li L, Wang X, Zhang Y (2014) Enhanced visible light-responsive photocatalytic activity of $LnFeO_3$ (Ln = La, Sm) nanoparticles by synergistic catalysis. Mater Res Bull 50:18
6. Zhang YW, Yang JX, Xu JF, Gao QY, Hong ZL (2012) Controllable synthesis of hexagonal and orthorhombic $YFeO_3$ and their visible-light photocatalytic activities. Mater Lett 81:1
7. Chen YY, Yang J, Wang XL, Feng FY, Zhang YM, Tang Y (2014) Synthesis $YFeO_3$ by salt-assisted solution combustion method and its photocatalytic activity. J Ceram Soc Jpn 122:146
8. Li L, Wang X (2016) Self-propagating combustion synthesis and synergistic photocatalytic activity of $GdFeO_3$ nanoparticles. J Solgel Sci Technol 79:107
9. Baeissa ES (2016) Environmental remediation of aqueous methyl orange dye solution via photocatalytic oxidation using Ag-$GdFeO_3$ nanoparticles. J Alloys Compd 678:267

10. Yang H, Zhang JX, Lin GJ, Xian T, Jiang JL (2013) Preparation, characterization and photocatalytic properties of terbium orthoferrite nanopowder. Adv Powder Technol 24:242
11. Zhou M, Yang H, Xian T, Zhang CR (2015) A new photocatalyst of $LuFeO_3$ for the dye degradation. Phys Scr 90:085808
12. Ding JL, Lu XM, Shu HM, Xie JM, Zhang H (2010) Microwave-assisted synthesis of perovskite $ReFeO_3$ (Re: La, Sm, Eu, Gd) photocatalyst. Mater Sci Eng B Adv 171:31
13. Parida KM, Reddy KH, Martha S, Das DP, Biswal N (2012) Fabrication of nanocrystalline $LaFeO_3$: An efficient sol-gel auto-combustion assisted visible light responsive photocatalyst for water decomposition. Int J Hydrogen Energ 35:12161
14. Tijare SN, Joshi MV, Padole PS, Mangrulkar PA, Rayalu SS, Labhsetwar NK (2012) Photocatalytic hydrogen generation through water splitting on nano-crystalline $LaFeO_3$ perovskite. Int J Hydrogen Energy 37:10451
15. Thirumalairajan S, Girija K, Ganesh I, Mangalaraj D, Viswanathan C, Balamurugan A, Ponpandian N (2012) Controlled synthesis of perovskite $LaFeO_3$ microsphere composed of nanoparticles via self-assembly process and their associated photocatalytic activity. Chem Eng J 209:420
16. Thirumalairajan S, Girija K, Hebalkar NY, Mangalaraj D, Viswanathan C, Ponpandian N (2013) Shape evolution of perovskite $LaFeO_3$ nanostructures: a systematic investigation of growth mechanism, properties and morphology dependent photocatalytic activities. RSC Adv 3:7549
17. Tang P, Tong Y, Chen H, Cao F, Pan G (2013) Microwave-assisted synthesis of nanoparticulate perovskite $LaFeO_3$ as a high active visible-light photocatalyst. Curr Appl Phys 13:340
18. Thirumalairajan S, Girija K, Mastelaro VR, Ponpandian N (2014) Photocatalytic degradation of organic dyes under visible light irradiation by floral-like $LaFeO_3$ nanostructures comprised of nanosheet petals. New J Chem 38:5480
19. Kumar RD, Jayavel R (2014) Facile hydrothermal synthesis and characterization of $LaFeO_3$ nanospheres for visible light photocatalytic applications. J Mater Sci Mater Electron 25:3953
20. Abazari R, Sanati S, Saghatforoush LA (2014) A unique and facile preparation of lanthanum ferrite nanoparticles in emulsion nanoreactors: Morphology, structure, and efficient photocatalysis. Mater Sci Semicond Process 25:301
21. Gaikwad VM, Sheikh JR, Acharya SA (2015) Investigation of photocatalytic and dielectric behavior of $LaFeO_3$ nanoparticles prepared by microwave-assisted sol–gel combustion route. J Solgel Sci Technol 76:27
22. Shen H, Xue T, Wang Y, Cao G, Lu Y, Fang G (2016) Photocatalytic property of perovskite $LaFeO_3$ synthesized by sol-gel process and vacuum microwave calcination. Mater Res Bull 84:15
23. Hu R, Li C, Wang X, Sun Y, Jia H, Su H, Zhang Y (2012) Photocatalytic activities of $LaFeO_3$ and La_2FeTiO_6 in p-chlorophenol degradation under visible light. Catal Commun 29:35
24. Wei Z-X, Wang Y, Liu J-P, Xiao C-M, Zeng W-W (2012) Synthesis, magnetization and photocatalytic activity of $LaFeO_3$ and $LaFe_{0.5}Mn_{0.5-x}O_{3-\delta}$. Mater Chem Phys 136:755
25. Li J, Pan X, Xu Y, Jia L, Yi X, Fang W (2015) Synergetic effect of copper species as cocatalyst on $LaFeO_3$ for enhanced visible-light photocatalytic hydrogen evolution. Int J Hydrogen Energy 40:13918
26. Xian T, Yang H, Huo YS, Ma JY, Zhang HM, Su JY, Feng WJ (2016) Fabrication of Ag-decorated $CaTiO_3$ nanoparticles and their enhanced photocatalytic activity for dye degradation. J Nanosci Nanotechnol 16:570
27. Okuno T, Kawamura G, Muto H, Matsuda A (2016) Photocatalytic properties of Au-deposited mesoporous SiO_2-TiO_2 photocatalyst under simultaneous irradiation of UV and visible light. J Solid State Chem 235:132
28. Lee KT, Chuah XF, Cheng YC, Lu SY (2015) Pt coupled $ZnFe_2O_4$ nanocrystals as a breakthrough photocatalyst for Fenton-like processes-photodegradation treatments from hours to seconds. J Mater Chem A 3:18578
29. Li S, Zhao Y, Wang C, Li D, Gao K (2016) Fabrication and characterization unique ribbon-like porous Ag/$LaFeO_3$ nanobelts photocatalyst via electrospinning. Mater Lett 170:122
30. Zhou M, Yang H, Xian T, Li RS, Zhang HM, Wang XX (2015) Sonocatalytic degradation of RhB over $LuFeO_3$ particles under ultrasonic irradiation. J Hazard Mater 289:149
31. Li K, Wang D, Wu F, Xie T, Li T (2000) Surface electronic states and photovoltage gas-sensitive characters of nanocrystalline $LaFeO_3$. Mater Chem Phys 64:269
32. Konstantinou IK, Albanis TA (2004) TiO_2-assisted photocatalytic degradation of azo dyes in aqueous solution: kinetic and mechanistic investigations: A review. Appl Catal B 49:1
33. Teoh WY, Scott JA, Amal R (2012) Progress in heterogeneous photocatalysis: from classical radical chemistry to engineering nanomaterials and solar reactors. J Phys Chem Lett 3:629
34. Xian T, Yang H, Di LJ, Dai JF (2015) Enhanced photocatalytic activity of $BaTiO_3$@g-C_3N_4 for the degradation of methyl orange under simulated sunlight irradiation. J Alloys Compd 622:1098
35. Morrison SR (1980) Electrochemistry at semiconductor and oxidized metal electrode. Plenum, NewYork, NY
36. Hotop H, Lineberger WC (1975) Binding energies in atomicnegative ions. J Phys Chem Ref Data 4:539
37. Andersen T, Haugen HK, Hotop H (1999) Binding energies in atomic negative ions: III. J Phys Chem Ref Data 28:1511
38. Kamat PV (2007) Meeting the clean energy demand: nanostructure architectures for solar energy conversion. J Phys Chem C 111:2834
39. Tachikawa T, Fujitsuka M, Majima T (2007) Mechanistic insight into the TiO_2 photocatalytic reactions: design of new photocatalysts. J Phys Chem C 111:5259
40. Jiang HY, Cheng K, Lin J (2012) Crystalline metallic Au nanoparticle-loaded alpha-Bi_2O_3 microrods for improved photocatalysis. Phys Chem Chem Phys 14:12114
41. Arai T, Yanagida M, Konishi Y, Iwasaki Y, Sugihara H, Sayama K (2007) Efficient complete oxidation of acetaldehyde into CO_2 over $CuBi_2O_4$/WO_3 composite photocatalyst under visible and UV light irradiation. J Phys Chem C 111:7574